

Correlation effects in focused transmission through disordered media

Chia Wei Hsu,¹ Seng Fatt Liew,¹ Arthur Goetschy,² Hui Cao,¹ and A. Douglas Stone¹

¹*Department of Applied Physics, Yale University, New Haven, Connecticut 06520, USA**

²*ESPCI ParisTech, PSL Research University, CNRS,
Institut Langevin, 1 rue Jussieu, F-75005 Paris, France*

By controlling the many degrees of freedom in the incident wavefront, one can manipulate wave propagation in complex and disordered structures. Such wavefront-shaping methods have been used extensively for controlling how much light is transmitted into wavelength-scale regions (speckles), a property that is insensitive to correlations in the speckle pattern. The extent to which coherent control is possible for larger regions depends strongly on such correlations and is of great interest for applications. With optical wavefront-shaping experiments and a filtered random matrix theory appropriate for open geometries, we show that long-range correlations in coherent diffusion substantially increase the range of control over transmission onto larger target regions, specifically when the number M_2 of targeted speckles exceeds g , the analog of the dimensionless conductance for electron waves. We find several statistical properties of coherent control to obey universal scaling laws when expressed in terms of M_2/g . Our work elucidates the critical role of speckle correlations in coherent control and provides a general theoretical framework for describing open diffusion in wavefront-shaping experiments.

Waves propagating through a disordered medium undergo multiple scattering from the inhomogeneities. Interference among the multiply scattered fields has important consequences that cannot be described with incoherent diffusion^{1,2}. By controlling the incident wave (“wavefront shaping,” WFS), one can manipulate this interference and drastically modify the transport of light, microwaves, and acoustic waves³. One early and notable example is focusing light onto a *local* speckle-sized target through aligning the scattered fields there^{4–7}, which has led to advances in imaging within biological tissue and other scattering materials⁸. The transport through disordered structures is described by a random field transmission matrix, and the use of WFS over such local properties has treated the matrix elements as having only short-range correlations on the scale of a single speckle^{4,9–13}. However, it has long been known that diffusive waves also exhibit long-range and infinite-range correlations^{14–17}; this was previously noted in the context of electron transport through mesoscopic structures, where correlations lead to anomalously large conductance fluctuations¹⁸. The long-range correlations are related to the existence of near-unity-transmission input states (“open channels”)^{19–25}, and have measurable effects on other *global* statistical properties of diffusive waves such as the total transmission variance^{26–29}, the increased background for maximally focused waves^{30–33}, and the singular values of large transmission matrices^{34–37}. With the emerging field of WFS, an important question, both scientifically and technologically, is how correlations affect the coherent control over targets larger than a single speckle and smaller than the full transmitted pattern, *i.e.* in between local and global. This intermediate regime remains poorly understood but is relevant for many applications ranging from telecommunications and cryptography to photothermal therapy and the optical or ultrasound imaging of large objects behind a scattering medium.

Here, we demonstrate the effects of correlations by means of optical WFS experiments in this interesting regime. WFS enables dynamic control over how much light is transmitted into a given target, and we find that for large targets, correlations increase the range of control significantly beyond what would be achievable if correlations were negligible (as is typically assumed). Physically this is because in a multiply scattering medium, the transmitted flux is carried by roughly only g open channels^{19–22}; here g is the analog of the dimensionless conductance or Thouless number for electron transport in a waveguide, and its definition in an open geometry will be discussed below. When the target region is large enough that the number M_2 of speckles in it exceeds g , the output channels are necessarily correlated. Such positive correlations reduce the effective degrees of freedom $M_2^{(\text{eff})}$ that need to be controlled and lead to the increased dynamic range and other correlation effects.

WFS experiments on strongly scattering media are typically performed in an open geometry: the illumination spot spreads laterally as wave diffuses into the medium. A rigorous random matrix theory for such a set-up was not known until recently, when the “filtered random matrix” ensemble (FRM) was introduced³⁸ and conjectured to apply to diffusion with an open boundary²³. There were some partial tests of the FRM eigenvalue distributions^{34–36}, but not with lateral diffusion accounted for rigorously. Here we show precisely how the FRM can be applied to an arbitrary open diffusion experiment, and confirm its predictions for the full distributions of transmission eigenvalues. We prove that the ratio M_2/g determines the presence or absence of significant correlation effects and derive new scaling laws for measurable statistical quantities that are found to agree very well with our experimental data. This theoretical framework is applicable to the WFS for light as well as microwaves and acoustic waves.

When we modulate M_1 incident channels with a spatial

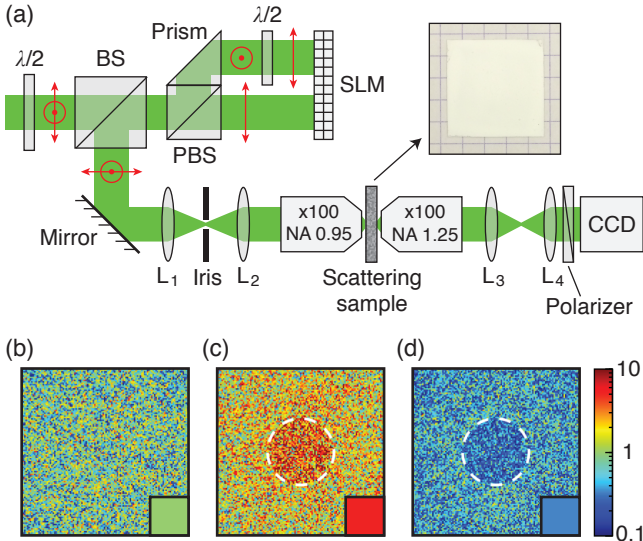


Figure 1. Experimental set-up and representative outputs. (a) A phase-only spatial light modulator (SLM) generates the desired incident wavefront and, together with a CCD camera, measures the optical transmission matrix. The scattering sample has average transmission $\bar{T} \approx 3\%$, with a picture shown in the inset. $\lambda/2$, half-wave plate; BS, beam splitter; PBS, polarizing beam splitter; L_1 – L_4 , lenses. (b–d) Output pattern on the CCD for a random wavefront (b) and for wavefronts optimized for maximal (c) and minimal (d) transmission into a target region containing $M_2 \approx 1700$ channels (within the white dashed circle), in saturated log scale; square on the corner indicates the average intensity inside the target.

light modulator (SLM) and collect M_2 channels transmitted into a target region, the input-output relation can be written as $|\psi_{\text{out}}\rangle = \tilde{t}|\psi_{\text{in}}\rangle$ where $|\psi_{\text{in}}\rangle$ and $|\psi_{\text{out}}\rangle$ are vectors of length M_1 and M_2 that contain the input and output field amplitudes. Here \tilde{t} is an M_2 -by- M_1 transmission matrix, and we use the tilde to indicate that it is filtered from a larger matrix by omitting columns/rows that correspond to the input/output channels not modulated/detected³⁸. The total flux into the focal target is $T = \langle\psi_{\text{out}}|\psi_{\text{out}}\rangle = \langle\psi_{\text{in}}|\tilde{t}^\dagger\tilde{t}|\psi_{\text{in}}\rangle$; the variational principle guarantees that the maximal and minimal transmitted fluxes are the extremal eigenvalues of $\tilde{t}^\dagger\tilde{t}$. The corresponding eigenvectors are the optimal input wavefronts that the SLM should generate. Thus the variance $\text{Var}(\tilde{\tau})$, where $\tilde{\tau}$ denotes the eigenvalues of $\tilde{t}^\dagger\tilde{t}$, is a measure of the dynamic range of focused transmission that is achievable by WFS. If the matrix elements of \tilde{t} were uncorrelated random numbers, for sufficiently large M_1 and M_2 the eigenvalues would follow the Marčenko–Pastur (MP) distribution³⁹, which has variance $\text{Var}(\tilde{\tau}^{(\text{MP})}) = \langle\tilde{\tau}\rangle^2 M_1/M_2$. The ratio between $\text{Var}(\tilde{\tau})$ and $\text{Var}(\tilde{\tau}^{(\text{MP})})$ is a measure of how correlations affect the range of coherent control.

We study the transport through a slab of zinc oxide (ZnO) microparticles (median diameter ≈ 200 nm) de-

posited on a cover slip, with slab thickness $L \approx 60 \mu\text{m}$ and total transmission $\bar{T} \approx 3\%$. The incident wavefront (wavelength $\lambda = 532 \text{ nm}$) is modulated with a phase-only SLM and then focused onto the sample with a high-NA objective, and the transmitted light is collected on a CCD camera; see the schematic illustration in Fig. 1a and details in Supplementary Information (SI) sections I–II. In our set-up, the SLM/CCD pixels modulate/detect different angles incident onto/transmitted from the sample. The nearby SLM pixels are grouped into macropixels; smaller macropixels correspond to more finely spaced incident angles, with a larger illumination spot and more available input channels. The illumination spot size determines the crucial parameter g in an open geometry, and we consider three macropixel sizes that correspond to illumination diameters $D_{\text{in}} \approx 6, 12, 24 \mu\text{m}$; the number of modes we modulate is $M_1 = 128, 512, 2048$ respectively. Our output speckle grains are slightly larger than one CCD pixel (the intensity autocorrelation width is 1.5 pixels on average), and we keep only one pixel out of 2×2 pixels in the data recorded on the CCD to remove correlations among neighboring pixels; thus each remaining CCD pixel corresponds to one output channel, free of short-range correlations. With this set-up, we measure the transmission matrix \tilde{t} using a phase-shifting common-path interferometric method (SI section III). Once the transmission matrix is measured, we use it to predict the optimal phase-only wavefront for a given target (SI section IV), and then measure the output on the CCD when such a wavefront is applied on the SLM. Exemplary outputs for enhanced and suppressed transmission into a large target are shown in Fig. 1b–d.

From the measured transmission matrices, we obtain the intensity correlation function between the output channels (SI section V and Supplementary Fig. 1), which shows the long-range contributions. Such long-range correlations explain why in Fig. 1b–d, the background speckle intensities outside the target increase (or decrease) with those inside the target, a phenomenon that has been observed previously^{30–33}.

For circular targets of varying sizes, we obtain the eigenvalues of $\tilde{t}^\dagger\tilde{t}$ from the measured transmission matrices. As the target region grows, the eigenvalue variance becomes larger than the uncorrelated MP variance, as shown in Fig. 2a. For small targets ($M_2 \lesssim 10^3$), we observe $\text{Var}(\tilde{\tau}) \approx \text{Var}(\tilde{\tau}^{(\text{MP})})$ with no obvious correlation effects, consistent with prior work involving small transmission matrices^{9–13}. However, for large targets ($M_2 \gtrsim 10^3$), $\text{Var}(\tilde{\tau})$ becomes significantly larger than $\text{Var}(\tilde{\tau}^{(\text{MP})})$, indicating an enhanced range of control due to correlations. The ratio between the eigenvalue range $\tilde{\tau}_{\text{max}} - \tilde{\tau}_{\text{min}}$ and that from an uncorrelated matrix $\tilde{\tau}_{\text{max}}^{(\text{MP})} - \tilde{\tau}_{\text{min}}^{(\text{MP})}$ is shown in Supplementary Fig. 2 (SI section VI), and it follows the same trend as the eigenvalue variance.

We now examine more detailed data for illumination diameter $D_{\text{in}} \approx 12 \mu\text{m}$. Figure 3 shows that the extremal eigenvalues $\tilde{\tau}_{\text{max}}$ and $\tilde{\tau}_{\text{min}}$ (green filled sym-

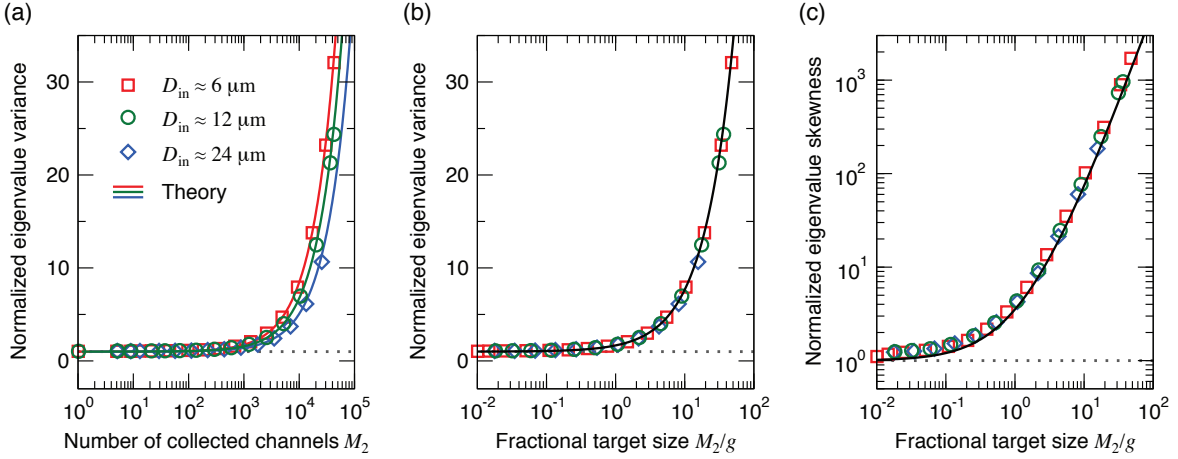


Figure 2. Emergence of correlation effects and scaling laws. (a) Variance of the transmission eigenvalues normalized by that of an uncorrelated matrix, $\text{Var}(\tilde{\tau})/\text{Var}(\tilde{\tau}^{(\text{MP})})$. Strong deviations from the uncorrelated behavior (namely, departure from unity, dotted line) arise when the target size M_2 exceeds the dimensionless conductance g (values given in the text). Symbols are experimental data with different illumination diameters D_{in} , and lines are equations (2). (b) Same as (a) but plotted against M_2/g , showing the universal scaling behavior. (c) Normalized eigenvalue skewness, $\text{Skew}(\tilde{\tau})/\text{Skew}(\tilde{\tau}^{(\text{MP})})$, which also follows a universal scaling curve; black line is equation (3).

bol) extend a wider range than the uncorrelated ones $\tilde{\tau}_{\text{max/min}}^{(\text{MP})} = \langle \tilde{\tau} \rangle (1 \pm \sqrt{M_1/M_2})^2$ (gray dot-dashed lines), and the difference grows with M_2 . We can readily achieve this extended range experimentally: when $M_2 \gtrsim 3000$, the largest and the smallest focused transmission reached with our phase-only SLM (red crosses) cover a wider range than the uncorrelated extrema, even though the uncorrelated extrema were calculated assuming both phase and amplitude modulations. Having access to the transmission matrix is important as it helps us find near-optimal wavefronts (SI section IV); a recent experiment³³ used feedback-based optimization and reported enhancements lower than the uncorrelated value $\tilde{\tau}_{\text{max}}^{(\text{MP})}/\langle \tilde{\tau} \rangle$ because it did not reach a near-optimal wavefront.

The full distributions of eigenvalues are shown in Fig. 4 for two representative target sizes. When $M_2 \approx 10^3$, the experimental distribution already differs detectably from the uncorrelated MP law (Fig. 4a). With a much larger target of $M_2 \approx 4 \times 10^4$, the experimental distribution spreads five times the width of the corresponding MP distribution (Fig. 4b)—a drastic change due to correlations.

To understand and to describe quantitatively these correlation effects, we make the following ansatz:

- The M_2 -by- M_1 partial transmission matrix \tilde{t} of an open disordered slab measured with a finite illumination area can be treated as a filtered matrix drawn from a larger N_2 -by- N_1 full transmission matrix t of a disordered coherent conductor in a closed waveguide of non-uniform width.

The parameters of the unknown full matrix t account for the effects of finite illumination area and lateral diffusion

in an open geometry, and they remain to be determined. It is known that for closed diffusive waveguides in the absence of absorption, $t^\dagger t$ has a bimodal eigenvalue density^{19–21}

$$p_{t^\dagger t}(\tau) = \frac{\bar{T}}{2\tau\sqrt{1-\tau}} \quad (1)$$

that is universal^{22,40,41} and parametrized only by the average transmission \bar{T} ; this allows us, using the FRM, to predict the statistical properties of \tilde{t} .

Equation (1) differs drastically from the MP distribution³⁹, indicating that the matrix elements of t are necessarily correlated. In particular, this asymmetric bimodal distribution indicates that the transmitted waves consist mainly of a relatively small number, $g \ll N_1$, of “open” eigenchannels with order-unity transmission ($\tau \approx 1$), while most of the other eigenchannels have $\tau \approx 0$ and barely contribute to transmission. The available degrees of freedom at the output is not the number of output channels defined by the geometry, N_2 , but rather it is approximately $g \equiv \langle \text{Tr}(t^\dagger t) \rangle = N_1 \bar{T}$; more precisely, it can be defined by the participation number $\langle (\sum_{n=1}^{N_1} \tau_n)^2 / (\sum_{n=1}^{N_1} \tau_n^2) \rangle$ (refs. 31, 32, and 42), which is $3g/2$ for the bimodal distribution in equation (1). If we collect more output channels than the available degrees of freedom at the output (namely, when $M_2 > 3g/2$), we expect to see strong correlation effects.

The intuitive discussion in the preceding paragraph can be made quantitative by using the analytic FRM formalism³⁸ to describe the matrix filtering process in our ansatz. In general, this requires knowing the three parameters N_1, N_2, \bar{T} of the unknown matrix t , in addition to the known size M_1, M_2 of the measured matrix \tilde{t} . But

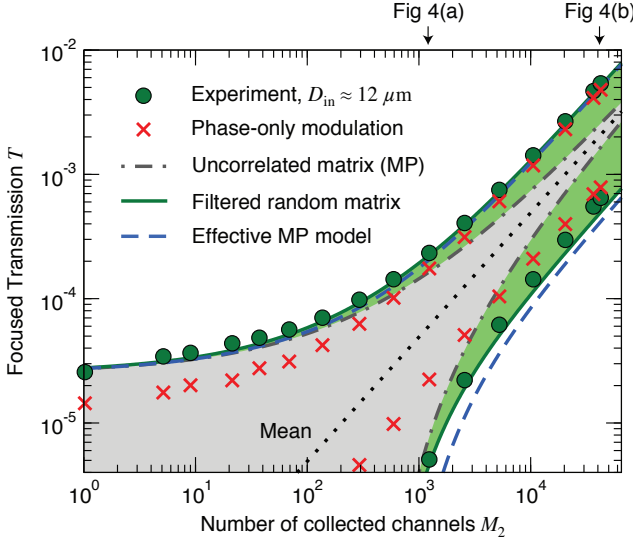


Figure 3. Allowed and achieved range of focused transmission as a function of the target size. The allowed range is given by the extremal eigenvalues of the measured transmission matrix (green circles). The achieved range through phase-only wavefront modulation is slightly narrower (red crosses) but still exceeds the Marčenko-Pastur (MP) law for uncorrelated matrices (gray shading) when the target is large. This deviation from the uncorrelated behavior is well described by theoretical predictions using the filtered random matrices (green shading) and the effective MP model (blue dashed lines).

for thick samples (specifically, when $\bar{T} \ll 2/3$, which is always the case in the diffusive regime), our derivation (SI section VII) shows that the variance normalized to the uncorrelated MP variance is simply

$$\frac{\text{Var}(\tilde{\tau})}{\text{Var}(\tilde{\tau}^{(\text{MP})})} = 1 + \frac{2M_2}{3g}, \quad (2)$$

which depends on a single parameter, M_2/g (recall that $\text{Var}(\tilde{\tau}^{(\text{MP})}) = \langle \tilde{\tau} \rangle^2 M_1/M_2$). As expected, when the target region contains more than $3g/2$ channels, the eigenvalues exhibit substantially more variation than the uncorrelated MP behavior, leading to a wider-than-expected dynamic range for coherent control.

To compare the experimental data with equation (2), the only parameter we need is the dimensionless conductance g . For a fixed input, the intensity correlation between far-away output speckles equals $2/(3g)$ (refs. 14–16), allowing us to determine g from the experimental correlation functions (Supplementary Fig. 1). We also determine g through the measured variance of the normalized total transmission (as in refs. 26 and 28), which also equals $2/(3g)$. The two methods yield almost the same values of g , whose average values are $g = 894 \pm 26, 1164 \pm 38, 1642 \pm 82$ for the three illumination sizes $D_{\text{in}} \approx 6, 12, 24 \mu\text{m}$ considered here (SI section VIII). Analytic expressions of g for an open geometry^{23,26,28,43,44} predict similar values, which we describe

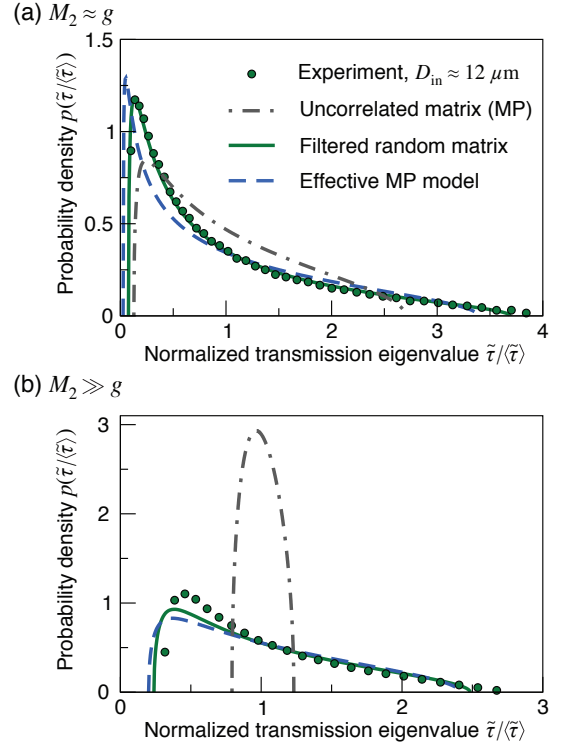


Figure 4. Full distributions of transmission eigenvalues. The two panels show the mean-normalized distributions for two target sizes: $M_2 \approx 10^3 \approx g$ (a), and $M_2 \approx 4 \times 10^4 \gg g$ (b). The experimental data (green circles; averaged over 10 data sets) differ from the uncorrelated MP law (gray dot-dashed lines) but are described accurately by the filtered random matrix theory (green solid lines) and approximately by the effective MP model (blue dashed lines).

in SI section IX.

With g determined, we compare equation (2) to the eigenvalue variance without any free parameter and observe excellent quantitative agreement (Fig. 2a). Equation (2) reveals that the MP-normalized eigenvalue variance follows a scaling law with respect to a single-parameter M_2/g , which we plot in Fig. 2b. Furthermore, we show in SI section VII that when $\bar{T} \ll 4/15$, the third central moment $\text{Skew}(\tilde{\tau}) \equiv \langle (\tilde{\tau} - \langle \tilde{\tau} \rangle)^3 \rangle$ of the eigenvalues also follows a single-parameter scaling law

$$\frac{\text{Skew}(\tilde{\tau})}{\text{Skew}(\tilde{\tau}^{(\text{MP})})} = 1 + \frac{2M_2}{g} + \frac{8M_2^2}{15g^2} \quad (3)$$

once normalized by the eigenvalue skewness of an uncorrelated matrix, $\text{Skew}(\tilde{\tau}^{(\text{MP})}) = \langle \tilde{\tau} \rangle^3 (M_1/M_2)^2$. Again M_2/g sets the departure from the uncorrelated behavior. This scaling is validated with the experimental data in Fig. 2c, again with no free parameter. In SI section VII, we also calculate the MP-normalized fourth central moment (kurtosis) and find that in general it depends on two parameters M_2/g and M_2/M_1 , with the dependence on M_2/M_1 dropping out when it is small; this is validated with experimental data in Supplementary Fig. 3.

We can also calculate the full distributions of the eigenvalues with the analytic FRM formalism. For the parameters of the unknown matrix t in our ansatz, we use the measured average transmission $\bar{T} = 3\%$, take $N_1 = g/\bar{T}$, and $N_2 \approx 6 \times 10^5$ as the number of CCD pixels when output collection is complete; note that N_1 is not simply the number of modes in the illumination area because g is enlarged by the lateral diffusion in an open geometry (SI section IX). The predicted eigenvalue distribution of the filtered matrix $\tilde{t}^\dagger \tilde{t}$ and its extremal values are obtained by solving equations (S9) and (S14) in SI section VII. These predictions, plotted in Figs. 3–4 as green solid lines, show excellent agreement with the experimental data (green circles) and striking difference from the uncorrelated MP law (gray dot-dashed lines).

A heuristic model which captures approximately the results of the FRM analysis is as follows. The correlations reduce the degrees of freedom at the output, but have no effect on the input channels which are modulated independently by the M_1 SLM macropixels. This suggests modeling the correlated M_2 -by- M_1 matrix \tilde{t} with an uncorrelated $M_2^{(\text{eff})}$ -by- M_1 matrix $\tilde{t}^{(\text{eff})}$ that has fewer output channels $M_2^{(\text{eff})} \leq M_2$. By choosing

$$M_2^{(\text{eff})} = M_2 \left(1 + \frac{2M_2}{3g} \right)^{-1}, \quad (4)$$

we match the eigenvalue variance of this uncorrelated matrix with that of \tilde{t} given in equation (2). $M_2^{(\text{eff})}$ can be considered an effective degrees of freedom, and as expected, $M_2^{(\text{eff})} \approx M_2$ when $M_2 \ll g$, and $M_2^{(\text{eff})} \approx 3g/2$ when $M_2 \gg g$. Within this model, all statistical quantities of $\tilde{t}^{(\text{eff})}$ follow the simple MP law with the reduced $M_2^{(\text{eff})}$, and all correlation effects are encapsulated in this reduction (which only depends on M_2/g). For example, the correlation enhancement of control range $(\tilde{\tau}_{\max}^{(\text{eff})} - \tilde{\tau}_{\min}^{(\text{eff})}) / (\tilde{\tau}_{\max}^{(\text{MP})} - \tilde{\tau}_{\min}^{(\text{MP})})$ plotted in Supplementary Fig. 2 is simply $\sqrt{1 + 2M_2/3g}$ when $M_2^{(\text{eff})} > M_1$. For large targets ($M_2 \gg g$), the ratio $\tilde{\tau}_{\max/\min}^{(\text{eff})} / \langle \tilde{\tau}^{(\text{eff})} \rangle$ approaches $(1 \pm \sqrt{2M_1/3g})^2$ and becomes independent of M_2 , meaning that the achievable total transmission enhancement (as studied in ref. 23) is determined solely by M_1/g . Predictions of this “effective MP” model are shown in Figs. 3–4 for the extremal eigenvalues and the eigenvalue distributions, as well as in Supplementary Figs. 2–3 for the eigenvalue range and kurtosis.

In summary, we have shown that correlations in the diffusion of light can increase the dynamic range of coherent control in WFS experiments. Thus one may achieve

better-than-expected outcomes when delivering energy into multi-speckle-sized regions, such as a photodetector for optical communication. Meanwhile, non-local correlations will hinder the generation of independent random numbers⁴⁵ when more than g output channels are collected. The correlation effects depend on g and can be enhanced or suppressed by changing the illumination spot size D_{in} , either through the SLM macropixel size (as is done here) or by making the illumination out of focus^{28,29}. Note that the wavefront with optimal target intensity does not necessarily provide the optimal target-to-background contrast, which is relevant for imaging and photothermal therapy applications. The theory here is applicable to microwave and acoustic wave, for which smaller g can be readily achieved. Approaching the localized regime ($g \approx 1$), the correlations are even stronger⁴⁶; deep inside the localized regime ($g \ll 1$), a single input eigenchannel dominates the transmission^{37,47}, so the achievable transmission enhancement equals M_1 and becomes independent of the target size. Future work may extend the present formalism to broadband coherent control⁴⁸ and to reflection and absorption in open disordered systems^{35,40,49,50}.

Acknowledgements

We thank S. Popoff, Y. Bromberg, S. Knitter, R. Sarma, W. Xiong, F. Scheffold, E. Akkermans, and I. M. Vellekoop for helpful discussions, and the anonymous reviewers for their constructive comments. This work is supported by the National Science Foundation under grant No. DMR-1307632, DMR-1205307, and ECCS-1068642, and by the US Office of Naval Research under grant No. N00014-13-1-0649. A.G. acknowledges the support of LABEX WIFI (Laboratory of Excellence ANR-10-LABX-24) within the French Program “Investments for the Future” under reference ANR-10-IDEX-0001-02 PSL.

Author Contributions

C.W.H. and S.F.L. performed the experiment. C.W.H. analysed the data and developed the theory descriptions. A.G. proposed the effective MP model. H.C. and A.D.S. supervised the project. All authors discussed and interpreted the results. C.W.H. and A.D.S. wrote the manuscript with input from all authors.

Additional information

Supplementary information is available in the online version of the paper. Reprints and permissions information is available online at www.nature.com/reprints. Correspondence and requests for materials should be addressed to C.W.H. (chiawei.hsu@yale.edu).

Competing financial interests

The authors declare no competing financial interests.

* chiawei.hsu@yale.edu

¹ E. Akkermans and G. Montambaux, *Mesoscopic Physics of*

Electrons and Photons (Cambridge University Press, Cambridge, UK, 2007).

² P. Sheng, *Introduction to Wave Scattering, Localization and Mesoscopic Phenomena* (Springer-Verlag, Berlin, 2006), 2nd ed.

³ A. P. Mosk, A. Lagendijk, G. Lerosey, and M. Fink, *Nature Photon.* **6**, 283 (2012).

⁴ I. M. Vellekoop and A. P. Mosk, *Opt. Lett.* **32**, 2309 (2007).

⁵ Z. Yaqoob, D. Psaltis, M. S. Feld, and C. Yang, *Nature Photon.* **2**, 110 (2008).

⁶ C.-L. Hsieh, Y. Pu, R. Grange, and D. Psaltis, *Opt. Express* **18**, 12283 (2010).

⁷ D. B. Conkey and R. Piestun, *Opt. Express* **20**, 27312 (2012).

⁸ R. Horstmeyer, H. Ruan, and C. Yang, *Nature Photon.* **9**, 563 (2015).

⁹ R. Sprak, A. Tourin, J. de Rosny, and M. Fink, *Phys. Rev. B* **78**, 012202 (2008).

¹⁰ A. Aubry and A. Derode, *Phys. Rev. Lett.* **102**, 084301 (2009).

¹¹ S. M. Popoff, G. Lerosey, R. Carminati, M. Fink, A. C. Boccara, and S. Gigan, *Phys. Rev. Lett.* **104**, 100601 (2010).

¹² S. M. Popoff, G. Lerosey, M. Fink, A. C. Boccara, and S. Gigan, *New J. Phys.* **13** (2011).

¹³ A. Drémeau, A. Liutkus, D. Martina, O. Katz, C. Schülke, F. Krzakala, S. Gigan, and L. Daudet, *Opt. Express* **23**, 11898 (2015).

¹⁴ M. J. Stephen and G. Cwilich, *Phys. Rev. Lett.* **59**, 285 (1987).

¹⁵ S. Feng, C. Kane, P. A. Lee, and A. D. Stone, *Phys. Rev. Lett.* **61**, 834 (1988).

¹⁶ P. A. Mello, E. Akkermans, and B. Shapiro, *Phys. Rev. Lett.* **61**, 459 (1988).

¹⁷ P. Sebbah, B. Hu, A. Z. Genack, R. Pnini, and B. Shapiro, *Phys. Rev. Lett.* **88**, 123901 (2002).

¹⁸ P. A. Lee, A. D. Stone, and H. Fukuyama, *Phys. Rev. B* **35**, 1039 (1987).

¹⁹ O. N. Dorokhov, *Solid State Commun.* **51**, 381 (1984).

²⁰ Y. Imry, *Europhys. Lett.* **1**, 249 (1986).

²¹ P. A. Mello, P. Pereyra, and N. Kumar, *Ann. Phys.* **181**, 290 (1988).

²² Y. V. Nazarov, *Phys. Rev. Lett.* **73**, 134 (1994).

²³ S. M. Popoff, A. Goetschy, S. F. Liew, A. D. Stone, and H. Cao, *Phys. Rev. Lett.* **112**, 133903 (2014).

²⁴ B. Gérardin, J. Laurent, A. Derode, C. Prada, and A. Aubry, *Phys. Rev. Lett.* **113**, 173901 (2014).

²⁵ R. Sarma, A. G. Yamilov, S. Petrenko, Y. Bromberg, and H. Cao, *Phys. Rev. Lett.* **117**, 086803 (2016).

²⁶ J. F. de Boer, M. P. van Albada, and A. Lagendijk, *Phys. Rev. B* **45**, 658 (1992).

²⁷ M. Stoytchev and A. Z. Genack, *Phys. Rev. Lett.* **79**, 309 (1997).

²⁸ F. Scheffold, W. Härtl, G. Maret, and E. Matijević, *Phys. Rev. B* **56**, 10942 (1997).

²⁹ T. Strudley, T. Zehender, C. Blejean, E. P. A. M. Bakkers, and O. L. Muskens, *Nature Photon.* **7**, 413 (2013).

³⁰ I. M. Vellekoop and A. P. Mosk, *Phys. Rev. Lett.* **101**, 120601 (2008).

³¹ M. Davy, Z. Shi, and A. Z. Genack, *Phys. Rev. B* **85**, 035105 (2012).

³² M. Davy, Z. Shi, J. Wang, and A. Z. Genack, *Opt. Express* **21**, 10367 (2013).

³³ O. S. Ojambati, J. T. Hosmer-Quint, K.-J. Gorter, A. P. Mosk, and W. L. Vos (2016), arXiv:1606.05613.

³⁴ H. Yu, T. R. Hillman, W. Choi, J. O. Lee, M. S. Feld, R. R. Dasari, and Y. K. Park, *Phys. Rev. Lett.* **111**, 153902 (2013).

³⁵ H. Yu, K. Lee, and Y. Park, *Phys. Rev. B* **93**, 104202 (2016).

³⁶ D. Akbulut, T. Strudley, J. Bertolotti, E. P. A. M. Bakkers, A. Lagendijk, O. L. Muskens, W. L. Vos, and A. P. Mosk, *Phys. Rev. A* **94**, 043817 (2016).

³⁷ Z. Shi and A. Z. Genack, *Phys. Rev. Lett.* **108**, 043901 (2012).

³⁸ A. Goetschy and A. D. Stone, *Phys. Rev. Lett.* **111**, 063901 (2013).

³⁹ V. A. Marčenko and L. A. Pastur, *Math. USSR Sbornik* **1**, 457 (1967).

⁴⁰ A. Yamilov, S. Petrenko, R. Sarma, and H. Cao, *Phys. Rev. B* **93**, 100201 (2016).

⁴¹ C. Jin, R. R. Nadakuditi, and E. Michielssen (2015), arXiv:1503.03432.

⁴² N. Verrier, L. Depraeter, D. Felbacq, and M. Gross, *Phys. Rev. B* **93**, 161114 (2016).

⁴³ R. Pnini and B. Shapiro, *Phys. Rev. B* **39**, 6986 (1989).

⁴⁴ A. García-Martín, F. Scheffold, M. Nieto-Vesperinas, and J. J. Sáenz, *Phys. Rev. Lett.* **88**, 143901 (2002).

⁴⁵ A. Liutkus, D. Martina, S. Popoff, G. Chardon, O. Katz, G. Lerosey, S. Gigan, L. Daudet, and I. Carron, *Sci. Rep.* **4**, 5552 (2014).

⁴⁶ W. K. Hildebrand, A. Strybulevych, S. E. Skipetrov, B. A. van Tiggelen, and J. H. Page, *Phys. Rev. Lett.* **112**, 073902 (2014).

⁴⁷ A. Peña, A. Girschik, F. Libisch, S. Rotter, and A. A. Chabanov, *Nat. Commun.* **5**, 3488 (2014).

⁴⁸ C. W. Hsu, A. Goetschy, Y. Bromberg, A. D. Stone, and H. Cao, *Phys. Rev. Lett.* **115**, 223901 (2015).

⁴⁹ Y. D. Chong and A. D. Stone, *Phys. Rev. Lett.* **107**, 163901 (2011).

⁵⁰ S. F. Liew, S. M. Popoff, S. W. Sheehan, A. Goetschy, C. A. Schmuttenmaer, A. D. Stone, and H. Cao, *ACS Photonics* **3**, 449 (2016).

Supplementary Information

I. Experimental set-up

As illustrated in Fig. 1a of the main text, the expanded output beam from a continuous-wave Nd:YAG laser (Coherent, Compass 215M-50 SL, wavelength $\lambda = 532$ nm) is split into two parallel beams with orthogonal linear polarizations and equal intensity, using a half-wave-plate, a polarizing beam splitter (PBS), and a right-angle prism. The PBS and the prism are mounted in the same holder to eliminate relative phase fluctuations between the two beams. The two beams are modulated with different areas of a phase-only spatial light modulator (SLM) (Hamamatsu, X10468-01) and then recombined; a second half-wave plate matches the polarization of one beam to that of the SLM. Using a 4-f system (lenses L_1 and L_2 ; focal lengths = 21 cm), the surface of the SLM is imaged onto the entrance pupil of a microscope objective ($NA_{in} = 0.95$, Nikon CF Plan 100 \times), and the scattering sample is positioned at the focal plane of the objective. The transmitted light is collected with an oil-immersion objective ($NA_{out} = 1.25$, Edmund DIN Achromatic 100 \times), and the exit pupil of the objective is imaged onto a CCD camera (Allied Vision, Prosilica GC 660) through another 4-f system (lenses L_3 and L_4 ; focal lengths = 20 cm). In this way, the SLM pixels and the CCD pixels correspond to the different angles incident onto and transmitted from the sample. We place a polarizer in front of the CCD to collect only one output polarization.

The nearby SLM pixels are grouped into square macropixels; smaller macropixels correspond to more finely spaced incident angles, which yields a larger illumination spot and provides more input channels (macropixels) for modulation. For example, when one macropixel consists of 8 \times 8 SLM pixels, we have $M_1^{(tot)} = 978$ macropixels (489 per polarization) imaged onto the entrance pupil of the input objective and available to use. We measure the transmission matrix for the $M_1 = 512$ input channels (macropixels) at the center (16 \times 16 per polarization), using the other $M_1^{(ref)} = 466$ available macropixels as the reference (see section III). Then we can synthesize the desired wavefront by printing the specified phases onto the M_1 macropixels; at this stage the other available macropixels are “switched off” by displaying a high-spatial-frequency phase pattern, making them blocked by the iris placed at the Fourier plane of the lens L_1 .

For the theoretical prediction of the dimensionless conductance g (see section IX), we need to know the spatial size and profile of the illumination spot. In our set-up, the SLM macropixels are mapped to the space (k_x, k_y) of transverse wavevectors on the surface of the sample. Let $q \times q$ denote the size of one macropixel in the k space.

Then the intensity profile of the incident light is

$$I(x, y) \sim \text{sinc}^2(qx/2)\text{sinc}^2(qy/2). \quad (\text{S1})$$

The illumination area (as defined in section IX) is $A_{in} \equiv [\iint dx dy I(x, y)]^2 / \iint dx dy I^2(x, y) = (3\pi/q)^2$. The macropixels corresponding to wavevectors within a circle of radius $(2\pi/\lambda)NA_{in}$ will be able to enter the entrance pupil of the input objective, so through the available number of macropixels $M_1^{(tot)} = 2\pi(2\pi/\lambda)^2(NA_{in})^2/q^2$, we can determine the area $A_{in} = (3\pi/q)^2$. We then define the illumination spot size $D_{in} \equiv \sqrt{4A_{in}/\pi}$ as the diameter of a circle whose area equals A_{in} . In this study we use 16 \times 16-, 8 \times 8-, and 4 \times 4-sized macropixels, which correspond to $D_{in} \approx 6, 12, 24 \mu\text{m}$ in our set-up.

II. Sample preparation and characterization

We dissolve 6 grams of ZnO microparticle powder (Alfa Aesar Puratronic) into 3 mL of deionized water and 3 mL of ethanol, and sonicate the mixture in an ultrasonic bath for 30 minutes for thorough dispersion. The solution is then spin-coated onto a microscope cover slip (22 \times 22 mm 2 , thickness 0.15 mm) at 500 RPM and allowed to dry. The resulting sample is shown in the inset of Fig. 1a in the main text. Scanning electron microscopy shows that the ZnO particle diameters center around 200 nm. We use the center of the sample, where the thickness of the ZnO film is measured by a profilometer to be $L \approx 60 \mu\text{m}$, and the total transmission is measured with photodetector to be $\bar{T} \approx 3\%$. The transport mean free path is determined by coherent backscattering to be $0.64 \pm 0.1 \mu\text{m}$.

III. Transmission matrix measurement

We measure the transmission matrix \tilde{t} using a modified version of the phase-shifting common-path interferometric method^{1,2}. As in Refs. 1 and 2, we control M_1 macropixels on the SLM and switch on additional $M_1^{(ref)}$ macropixels with a flat phase as the reference. When the a -th input mode is sent in with a relative phase of ϕ , the measured intensity on the b -th pixel of the CCD is $|e^{i\phi}\tilde{t}_{ba} + s_b|^2$, where s_b denotes the transmitted field from the reference pixels. With four measurements at $\phi = 0, \pi/2, \pi, 3\pi/2$, we obtain $u_{ba} = \tilde{t}_{ba}s_b^*$. We perform the measurements with the input channels $\{a\}$ in the Hadamard basis, and then transform to the canonical basis so that $\{a\}$ correspond to the SLM macropixels (*i.e.* incident angles).

With the method above, what we obtain is the transmission matrix \tilde{t}_{ba} multiplied by an unwanted conjugated output field s_b^* from the reference. Therefore we know the

relative phase and amplitude between the input channels $\{a\}$ but not those between the output channels $\{b\}$. To study $\tilde{t}^\dagger \tilde{t}$ and the transmitted intensity, it is necessary to recover the relative amplitude between the output channels (the relative phase between $\{b\}$ is not relevant). Thus, for each input channel a , we perform an additional step where the $M_1^{(\text{ref})}$ reference pixels are switched off, and the CCD measures the transmitted intensity $|\tilde{t}_{ba}|^2$ from the M_1 control pixels only—this provides the relative amplitude between the output channels. Specifically, we use $u_{ba}|\tilde{t}_{ba}|/|u_{ba}|$ as our transmission matrix, which equals $\tilde{t}_{ba}s_b^*/|s_b|$ and contains the relative amplitude between the output channels. The whole measurement process takes 2, 8, 32 minutes respectively for $D_{\text{in}} \approx 6, 12, 24 \mu\text{m}$ (with $M_1 = 128, 512, 2048$), within the decorrelation time of the sample.

For each illumination diameter, we measure 10 transmission matrices at sufficiently different times that there is no discernible correlation between the measured matrices. The 10 sets of data are used to improve the statistics of the eigenvalues and the intensity correlations.

IV. Determination of optimal phase-only wavefront

Once the transmission matrix is measured, we can instantly determine the optimal wavefront for any given target; this is advantageous over feedback-based optimizations³, for which a separate experiment needs to be performed for each target.

When both amplitude and phase can be modulated, the wavefronts that produce the maximal and the minimal transmission into the target are simply the eigenvectors corresponding to the largest and the smallest eigenvalues of $\tilde{t}^\dagger \tilde{t}$. For phase-only modulation (as in our experiment), the optimal wavefront is no longer an eigenvector. We find that the phase part of the maximal eigenvector is generally a good approximation for the maximal-transmission phase-only wavefront. For minimal transmission, taking the phase of the minimal eigenvector is not optimal (for reasons explained in Ref. 4), so we use a nonlinear optimization instead. Specifically, we look for the phase profile $\{\phi_1, \dots, \phi_{M_1}\}$ that minimizes the figure of merit, $\text{FOM} = \sum_{b=1}^{M_2} |\tilde{t}_{ba} e^{i\phi_a}|^2$. After comparing the optimization algorithms implemented in the free optimization package NLOpt⁵, we chose the gradient-based low-storage BFGS algorithm^{6,7}. The optimization only takes a few seconds.

We then display the predicted optimal wavefront on the SLM and measure the output on the CCD. For maximal transmission, the measured output is typically very close to the prediction from \tilde{t} ; for minimal transmission, the agreement tends to be less good due to noise in \tilde{t} .

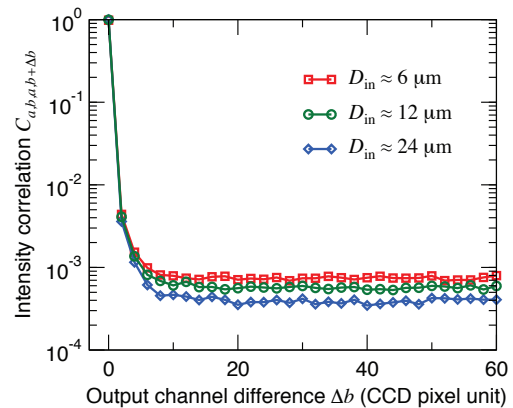
V. Speckle intensity correlations

The random speckle intensities exhibit non-local correlations, which lead to the enhanced dynamic control range with wavefront shaping. Let $T_{ab} \equiv |t_{ba}|^2$ denote the transmitted flux (namely, speckle intensity) from input channel a to output channel b . In the diffusive regime, the intensity correlations take on the form

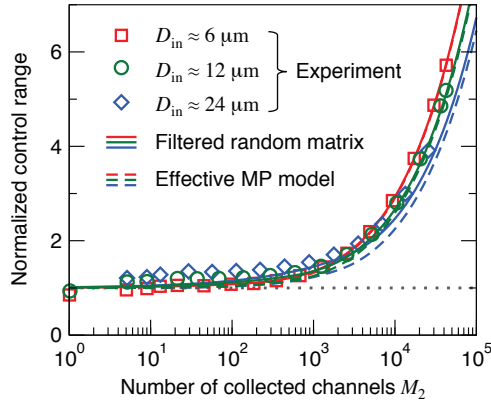
$$\begin{aligned} C_{ab,a'b'} &\equiv \frac{\langle T_{ab} T_{a'b'} \rangle}{\langle T_{ab} \rangle \langle T_{a'b'} \rangle} - 1, \\ &= C_{ab,a'b'}^{(1)} + C_{ab,a'b'}^{(2)} + C_{ab,a'b'}^{(3)}, \\ &\approx \delta_{aa'} \delta_{bb'} + \frac{2}{3g} (\delta_{aa'} + \delta_{bb'}) + \frac{2}{15g^2}, \end{aligned} \quad (\text{S2})$$

where the angular brackets denote ensemble average over different realizations of disorder. The terms $C^{(1)}$, $C^{(2)}$, $C^{(3)}$ are called short-range, long-range, and infinite-range correlations, for $C^{(1)}$ decays exponentially with the channel displacements $\Delta a \equiv a' - a$ and $\Delta b \equiv b' - b$, $C^{(2)}$ decays as a power law, and $C^{(3)}$ is independent of Δa and Δb . For a waveguide geometry with the incident wave covering the entire cross section, the dimensionless conductance g is given by $g \equiv \sum_{a,b} T_{ab}$ (summing over all waveguide modes), and the expressions for $C^{(1)}$, $C^{(2)}$, $C^{(3)}$ was derived in Ref. 8. For incident beams with a finite beam width, the form of $C^{(2)}$ is modified^{9–11}, resulting in g 's that depend on the illumination spot's size and shape (see section IX). The last line of Eq. (S2) is applicable when the channel differences Δa and Δb are large; it is also generally valid in quasi-1D geometries where all the input and output channels are statistically equivalent (isotropic assumption)^{12,13}. Refs. 14 and 15 review these correlation functions.

We can evaluate the intensity correlations from the experimentally measured transmission matrices \tilde{t}_{ba} . Here we are interested in the correlations among the output channels $\{b\}$ for a fixed input a , given by Eq. (S2) with



Supplementary Figure 1. Intensity correlation $C_{ab,a'b'}$ between two output speckles ($b' = b + \Delta b$), for a fixed input ($a = a'$), determined from the experimentally measured transmission matrices.



Supplementary Figure 2. Enhancement of the coherent control range due to long-range correlations, showing $\tilde{\tau}_{\max} - \tilde{\tau}_{\min}$ normalized by that of an uncorrelated matrix, $\tilde{\tau}_{\max}^{(\text{MP})} - \tilde{\tau}_{\min}^{(\text{MP})}$. Symbols are experimental data. Solid lines are the FRM predictions by solving Eq. (S14). Dashed lines are predictions of the effective MP model; for $D_{\text{in}} \approx 6, 12 \mu\text{m}$ they almost overlap with the solid lines.

$a' = a$ and $b' = b + \Delta b$. When $\Delta b = 0$, $C_{ab,ab} \approx 1$ is dominated by the short-range correlation (or, simply the speckle intensity fluctuation). When Δb is large, $C_{a,b,a,b+\Delta b} \approx 2/(3g)$ is dominated by the first term of $C^{(2)}$; note that this first term of $C^{(2)}$ is independent of Δb , so it is in fact infinite-ranged for Δb (even though $C^{(2)}$ is conventionally called long-range correlation).

When the ensemble average is approximated by averaging over K realizations, the uncertainty in $C_{ab,a'b'}$ is roughly $1/\sqrt{K}$. Therefore, to resolve the background of $2/(3g)$, one needs to average over a very large number $K \gg (3g/2)^2 \gtrsim 10^6$ of realizations. Also, small and unintended variation within the ensemble (*e.g.* measurements made at two sample locations where the thickness L differ slightly) can lead to an overestimate of $C_{ab,a'b'}$ (and subsequently an underestimate of g). To calculate $C_{a,b,a,b+\Delta b}$ from the transmission matrices we measured, for each b and each Δb , we replace the ensemble average with an average over the output intensity from 1000 random input wavefronts to ensure no artificial variation is introduced. Since the normalization by $\langle T_{ab} \rangle \langle T_{a'b'} \rangle$ removes the dependence on b and since the correlations should only depend on the magnitude of Δb , we average the resulting $C_{a,b,a,b+\Delta b}$ over 187×187 output channels $\{b\}$ in our data, the four displacement vectors

$\Delta b = (\Delta x, \Delta y), (\Delta x, -\Delta y), (-\Delta x, \Delta y), (-\Delta x, -\Delta y)$, and the 10 sets of transmission matrices we measured.

The resulting intensity correlation $C_{a,b,a,b+\Delta b}$ as a function of Δb is shown in Supplementary Fig. 1. A non-zero constant background persists for arbitrarily large Δb , meaning the output intensities at far-away pixels are still positively correlated. We use the height of this background to determine g (see section VIII).

VI. Plot of eigenvalue range

In Supplementary Fig. 2, we show the ratio between the eigenvalue range $\tilde{\tau}_{\max} - \tilde{\tau}_{\min}$ and that from an uncorrelated matrix $\tilde{\tau}_{\max}^{(\text{MP})} - \tilde{\tau}_{\min}^{(\text{MP})}$, comparing the experimental data with theory predictions given in section VII C.

VII. Filtered random matrix (FRM) formalism

Consider a M_2 -by- M_1 submatrix \tilde{A} of a larger N_2 -by- N_1 matrix A , and let Λ and $\tilde{\Lambda}$ denote the eigenvalues of the Hermitian matrices $A^\dagger A$ and $\tilde{A}^\dagger \tilde{A}$. For what we consider in the main text, $A = \tilde{t}$ is the measured transmission matrix, $A = t$ is an effective full matrix, the distribution of Λ is known, and we want to know the statistics of $\tilde{\Lambda}$.

When A is random and in the limit of N_1, N_2, M_1, M_2 going to infinity with arbitrary but finite fractions $m_1 \equiv M_1/N_1$, $m_2 \equiv M_2/N_2$, and $\alpha \equiv N_1/N_2$, we can treat this problem analytically with free probability theory. We write the filtered matrix as $\tilde{A} = P_2 A P_1$, where P_1 and P_2 are N_1 -by- M_1 and M_2 -by- N_2 rectangular matrices that project out the filtered columns and rows of the full matrix A , and define $\mathcal{P}_1 \equiv P_1 P_1^\dagger$ and $\mathcal{P}_2 \equiv P_2^\dagger P_2$. Ref. 16 considered the case when A is square ($\alpha = 1$) and derived the distribution of $\tilde{\Lambda}$. Here, we generalize to rectangular A 's (necessary for the open slab geometry where t is not square) and derive the higher moments of $\tilde{\Lambda}$.

A. Eigenvalue moments

The n -th moment of $\tilde{\Lambda}$ can be written as $\langle \tilde{\Lambda}^n \rangle = \langle \Lambda_{A^\dagger \mathcal{P}_2 A \mathcal{P}_1}^n \rangle / m_1$ and then expressed as the moments of $\Lambda_{A^\dagger \mathcal{P}_2 A}$ and $\Lambda_{\mathcal{P}_1}$ using the asymptotic freeness^{17,18} between $A^\dagger \mathcal{P}_2 A$ and \mathcal{P}_1 . Then, using $\langle \Lambda_{A^\dagger \mathcal{P}_2 A}^n \rangle = \langle \Lambda_{A A^\dagger \mathcal{P}_2}^n \rangle / \alpha$, the asymptotic freeness between $A A^\dagger$ and \mathcal{P}_2 , and $\langle \Lambda_{A A^\dagger}^n \rangle = \langle \Lambda_{A^\dagger A}^n \rangle \alpha$, we can express $\langle \tilde{\Lambda}^n \rangle$ with the moments of Λ . After some algebra, we obtain

$$\langle \tilde{\Lambda} \rangle = m_2 \langle \Lambda \rangle, \quad (S3)$$

$$\text{Var}(\tilde{\Lambda}) = m_1 m_2 [m_2 \text{Var}(\Lambda) + (1 - m_2) \alpha \langle \Lambda \rangle^2], \quad (S4)$$

$$\text{Skew}(\tilde{\Lambda}) = m_1^2 m_2 [m_2^2 \text{Skew}(\Lambda) + 3m_2(1 - m_2) \alpha \text{Var}(\Lambda) \langle \Lambda \rangle + (1 - m_2)(1 - 2m_2) \alpha^2 \langle \Lambda \rangle^3], \quad (S5)$$

$$\begin{aligned} \text{Kurt}(\tilde{\Lambda}) = m_1^2 m_2 & \{ m_1 m_2^3 \text{Kurt}(\Lambda) + 4m_1 m_2^2 (1 - m_2) \alpha \text{Skew}(\Lambda) \langle \Lambda \rangle \\ & + 2m_2^2 [m_1(1 - m_2) \alpha + (1 - m_1)m_2] \text{Var}(\Lambda)^2 + 2m_2(1 - m_2) \alpha [m_1(3 - 5m_2) \alpha + 2m_2] \text{Var}(\Lambda) \langle \Lambda \rangle^2 \\ & + (1 - m_2) \alpha^2 [m_1(1 - 5m_2 + 5m_2^2) \alpha + 2m_2(1 - m_2)] \langle \Lambda \rangle^4 \}, \end{aligned} \quad (S6)$$

with the variance being $\text{Var}(\tilde{\Lambda}) \equiv \langle (\tilde{\Lambda} - \langle \tilde{\Lambda} \rangle)^2 \rangle$, the skewness $\text{Skew}(\tilde{\Lambda}) \equiv \langle (\tilde{\Lambda} - \langle \tilde{\Lambda} \rangle)^3 \rangle$, and the kurtosis $\text{Kurt}(\tilde{\Lambda}) \equiv \langle (\tilde{\Lambda} - \langle \tilde{\Lambda} \rangle)^4 \rangle$. Eqs. (S3–S4) generalize Eqs. (S12–S13) in Ref. 16 to rectangular A 's. One may also write Eqs. (S4–S6) using $\langle \tilde{\Lambda}^n \rangle$ and $\langle \Lambda^n \rangle$, for which the expressions are longer but the symmetry between input m_1 and output

m_2 is more obvious.

The bimodal distribution in Eq. (1) of the main text has moments $\langle \tau \rangle = \bar{T}$, $\langle \tau^2 \rangle = (2/3)\bar{T}$, $\langle \tau^3 \rangle = (8/15)\bar{T}$, and $\langle \tau^4 \rangle = (16/35)\bar{T}$. Substituting these moments into Eqs. (S4–S6), we obtain Eqs. (2–3) of the main text for the single-parameter scaling of the MP-normalized variance and skewness, and

$$\frac{\text{Kurt}(\tilde{\tau})}{\text{Kurt}(\tilde{\tau}^{(\text{MP})})} = \left[1 + 4 \left(\frac{M_2}{g} + \frac{34M_2^2}{45g^2} + \frac{4M_2^3}{35g^3} \right) + \frac{2M_2}{M_1} \left(1 + \frac{4M_2}{3g} + \frac{4M_2^2}{9g^2} \right) \right] \left(1 + \frac{2M_2}{M_1} \right)^{-1} \quad (S7)$$

for the kurtosis, which is valid when $\bar{T} \ll 18/119$. Here, the uncorrelated kurtosis is $\text{Kurt}(\tilde{\tau}^{(\text{MP})}) = \langle \tilde{\tau} \rangle^4 (M_1/M_2)^3 (1 + 2M_2/M_1)^{19}$, and $g \equiv N_1 \bar{T}$ is the dimensionless conductance. In general, this MP-normalized kurtosis depends on both M_2/g and M_2/M_1 ; but when M_2/M_1 is small, it will only depend on M_2/g , similar to the MP-normalized variance and skewness in Eqs. (2–3) of the main text. Supplementary Fig. 3 compares the analytic prediction Eq. (S7) to the experimental data; we observe very good agreement with no fitting.

B. Eigenvalue distribution

The eigenvalue distribution $p_{\tilde{A}^\dagger \tilde{A}}(x)$ can be obtained through its resolvent (also called the Stieltjes transform) $g_{\tilde{A}^\dagger \tilde{A}}(z)$. The derivation for $g_{\tilde{A}^\dagger \tilde{A}}(z)$ follows the same procedure as in Ref. 16; the only difference is that Eq. (S9) of Ref. 16 becomes

$$\mathcal{S}_{A^\dagger \mathcal{P}_2 A \mathcal{P}_1}(z) = \mathcal{S}_{\mathcal{P}_2}(\alpha z) \mathcal{S}_{A^\dagger A}(z) \mathcal{S}_{\mathcal{P}_1}(z), \quad (S8)$$

where $\mathcal{S}_X(z)$ is the \mathcal{S} -transform of matrix X . Following the derivation in Ref. 16, we find $g_{\tilde{A}^\dagger \tilde{A}}(z)$ to be given by the solution of

$$L(z)g_{A^\dagger A}(N(z)L(z)/D(z)) = D(z), \quad (S9)$$

where

$$N(z) = zm_1 g_{\tilde{A}^\dagger \tilde{A}}(z) + 1 - m_1, \quad (S10)$$

$$L(z) = zm_1 g_{\tilde{A}^\dagger \tilde{A}}(z) + (1/\alpha) - m_1, \quad (S11)$$

$$D(z) = m_1 g_{\tilde{A}^\dagger \tilde{A}}(z) [zm_1 g_{\tilde{A}^\dagger \tilde{A}}(z) + (m_2/\alpha) - m_1]. \quad (S12)$$

Eqs. (S9–S12) generalize Eqs. (3–5) in Ref. 16 to rectangular A 's. Once the complex-valued $g_{\tilde{A}^\dagger \tilde{A}}(z)$ is obtained by numerically solving Eq. (S9), the desired eigenvalue distribution follows from the inverse Stieltjes transform, $p_{\tilde{A}^\dagger \tilde{A}}(x) = -\lim_{\epsilon \rightarrow 0^+} \text{Img}_{\tilde{A}^\dagger \tilde{A}}(x + i\epsilon)/\pi$.

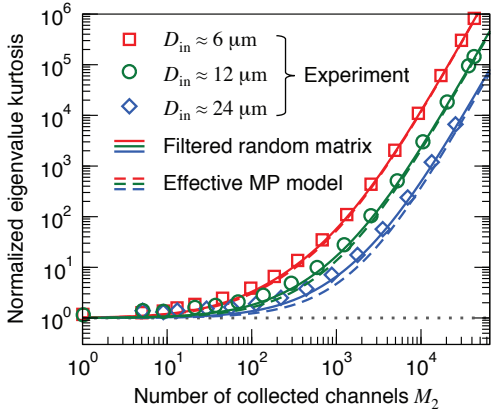
Note that when $m_2 = 1$, the dependence on the shape parameter α drops out. In general, the number $\alpha \equiv N_1/N_2$ for the shape of the full matrix A is important when only a small fraction of the output is collected, but it is inconsequential when m_2 is large; this explains why Ref. 20 (where $m_2 = 1$) and Ref. 21 (where $m_2 = 0.5$) modeled the full matrix A as being square but still obtained good agreement.

C. Extremal eigenvalues

The extremal eigenvalues of $\tilde{A}^\dagger \tilde{A}$ follow from the resolvent. From Eqs. (S9–S12), we can write

$$z = \frac{[\xi g_{A^\dagger A}(\xi) - p][\xi g_{A^\dagger A}(\xi) - q]}{g_{A^\dagger A}(\xi)[\xi g_{A^\dagger A}(\xi) - r]} \quad (S13)$$

where $\xi \equiv N(z)L(z)/D(z)$, $p \equiv 1 - m_1$, $q \equiv 1 - (m_2/\alpha)$, $r \equiv 1 - (1/\alpha)$. At the upper or lower edge ($z = z_0$) of the



Supplementary Figure 3. Normalized kurtosis of the eigenvalues, $\text{Kurt}(\tilde{\tau})/[(\tilde{\tau})^4(M_1/M_2)^3]$. Same convention as Supplementary Fig. 2.

distribution, the probability density becomes zero, and its slope diverges. That means $g_{\tilde{A}^\dagger \tilde{A}}(z_0)$ is purely real and $|g'_{\tilde{A}^\dagger \tilde{A}}(z_0)| = \infty$; this occurs when $\partial z/\partial \xi = 0$. Taking the ξ derivative of Eq. (S13), we see that $\partial z/\partial \xi = 0$ when

$$\begin{aligned} \frac{dg_{A^\dagger A}(\xi)}{d\xi} \Big|_{\xi=\xi_0} &= g_{A^\dagger A}^2(\xi_0) \times \\ & \frac{-pq + \xi_0^2 g_{A^\dagger A}^2(\xi_0) - r[2\xi_0 g_{A^\dagger A}(\xi_0) - p - q]}{pq[2\xi_0 g_{A^\dagger A}(\xi_0) - r] - (p + q - r)\xi_0^2 g_{A^\dagger A}^2(\xi_0)}. \end{aligned} \quad (\text{S14})$$

We solve Eq. (S14) for a real-valued ξ_0 , and plug it into Eq. (S13) to obtain the extremal eigenvalue z_0 . Typically, there will be two solutions of ξ_0 , which gives the minimal and the maximal eigenvalues. Eqs. (S13–S14) generalize Eqs. (S14–S15) in Ref. 16 to rectangular A 's.

D. Effective MP model

Here we provide more details on the heuristic effective MP model introduced in the main text, and write it in a more general setting that is not limited to the bimodal $p(\tau)$ distribution. In this model, instead of calculating the eigenvalues $\tilde{\Lambda}$ associated with the M_2 -by- M_1 matrix \tilde{A} which has correlated matrix elements in general, we calculate the eigenvalues $\tilde{\Lambda}^{(\text{eff})}$ associated with an uncorrelated $M_2^{(\text{eff})}$ -by- M_1 matrix $\tilde{A}^{(\text{eff})}$. Since the matrix elements of $\tilde{A}^{(\text{eff})}$ are uncorrelated, the eigenvalues $\tilde{\Lambda}^{(\text{eff})}$ follow the simple MP distribution¹⁹

$$p(x) = \frac{\sqrt{(\tilde{\Lambda}_{\max}^{(\text{eff})} - x)(x - \tilde{\Lambda}_{\min}^{(\text{eff})})}}{2\pi\gamma\langle\tilde{\Lambda}^{(\text{eff})}\rangle x} + \left(1 - \frac{1}{\gamma}\right)\theta(\gamma - 1)\delta(x), \quad (\text{S15})$$

where $\gamma \equiv M_1/M_2^{(\text{eff})}$, $\theta(\gamma - 1)$ is a step function, and $\delta(x)$ is the delta function. The first few central moments are $\text{Var}(\tilde{\Lambda}^{(\text{eff})}) = \langle\tilde{\Lambda}^{(\text{eff})}\rangle^2 M_1/M_2^{(\text{eff})}$,

Skew($\tilde{\Lambda}^{(\text{eff})}$) = $\langle\tilde{\Lambda}^{(\text{eff})}\rangle^3 (M_1/M_2^{(\text{eff})})^2$, Kurt($\tilde{\Lambda}^{(\text{eff})}$) = $\langle\tilde{\Lambda}^{(\text{eff})}\rangle^4 (M_1/M_2^{(\text{eff})})^3 [1 + 2(M_2^{(\text{eff})}/M_1)]$. By choosing

$$\langle\tilde{\Lambda}^{(\text{eff})}\rangle = m_2\langle\Lambda\rangle, \quad (\text{S16})$$

$$M_2^{(\text{eff})} = \frac{N_1 m_2 \langle\Lambda\rangle^2}{m_2 \text{Var}(\Lambda) + (1 - m_2)\alpha\langle\Lambda\rangle^2},$$

we match the first two moment of $\tilde{\Lambda}^{(\text{eff})}$ with those of $\tilde{\Lambda}$ given in Eqs. (S3–S4). Then, all other statistics of $\tilde{\Lambda}^{(\text{eff})}$ are given by the MP law above.

In the limit of small m_1 , the fourth central moment (kurtosis) also approaches that of $\tilde{\Lambda}$ given in Eq. (S6). In fact, numerical tests with random matrices with different distributions $p_{A^\dagger A}$ suggest that all even central moments of $\tilde{\Lambda}^{(\text{eff})}$ approach those of $\tilde{\Lambda}$ in the limit of small m_1 . However, the odd central moments of $\tilde{\Lambda}^{(\text{eff})}$ do not always approach those of $\tilde{\Lambda}$, as we can explicitly check by comparing the effective-MP skewness with Eq. (S5).

For the bimodal distribution discussed in the main text where we take $M_2^{(\text{eff})} = M_2/[1 + (2M_2/3g)]$, we can compare the effective-MP kurtosis to Eq. (S7) and see that the two agree when $M_1 \ll g$ (namely, when $m_1 \ll \bar{T}$). In our experiment, $M_1/g \approx 0.14, 0.44, 1.2$ for $D_{\text{in}} \approx 6, 12, 24 \mu\text{m}$, so we expect this effective MP model to work best for the smaller illumination diameters. Indeed, we compare this model to the FRM and the experimental data in Supplementary Figs. 2,3 for the eigenvalue range and kurtosis at different illumination diameters, and for $D_{\text{in}} \approx 6, 12 \mu\text{m}$ we barely see any difference between this model and the full FRM.

VIII. Experimental measurements of g

Here we determine g from the experimentally measured transmission matrices, through two methods. For a fixed input, the speckle intensity correlation $C_{ab,ab'}$ between two far-away output speckles is $2/(3g)$, as shown in Eq. (S2). We have already evaluated such $C_{a,b,a,b+\Delta b}$ from the experimentally measured transmission matrices in section V. The g 's given by equating the large- Δb data in Supplementary Fig. 1 to $2/(3g)$ are listed in Supplementary Table 1 as $g_{C^{(2)}}$; the indicated uncertainty is the standard deviation among the $g_{C^{(2)}}$'s at different Δb 's.

A related method to determine g is through the variance of the total transmission, $T_a = \sum_b T_{ab}$. By writing $\langle\delta T_a^2\rangle = \sum_b \sum_{b'} \langle\delta T_{ab} \delta T_{ab'}\rangle$ and summing over b and b' in Eq. (S2), we see that

$$\frac{\text{Var}(T_a)}{\langle T_a \rangle^2} = \frac{2}{3g} \quad (\text{S17})$$

in the diffusive regime where $\bar{T} \ll 1$. In Refs. 10, 11, 22, and 23, such total transmission measurements were used to determine g . Note that Eq. (S17) is also valid for the “partial transmission” into M_2 channels as long as $M_2 \gg g$. From the experimentally measured transmission matrices, we calculate the transmission into $M_2 = 247^2 \gg g$ independent CCD pixels and

| | $D_{\text{in}} \approx 6\mu\text{m}$ | $D_{\text{in}} \approx 12\mu\text{m}$ | $D_{\text{in}} \approx 24\mu\text{m}$ |
|---------------|--------------------------------------|---------------------------------------|---------------------------------------|
| $g_{C^{(2)}}$ | 897 ± 38 | 1163 ± 55 | 1691 ± 129 |
| g_{T_a} | 891 ± 35 | 1164 ± 53 | 1592 ± 100 |

Supplementary Table 1. Experimentally determined values of g from the $C^{(2)}$ part of the speckle intensity correlation and from the total transmission variance.

then evaluate g from its variance. Similar to our calculation of $C_{a,b,a,b+\Delta b}$ (section V), here we calculate the variance over 1000 random input wavefronts to avoid artificial variations in an ensemble average. The resulting g 's given by Eq. (S17) are listed in Supplementary Table 1 as g_{T_a} ; the indicated uncertainty is the standard deviation among the g_{T_a} 's obtained from the 10 sets of transmission matrices.

We take the average g from the two methods when comparing the FRM theory to our experimental data, namely in Figs. 2-4 of the main text and in Supplementary Figs. 2-3.

IX. Theoretical predictions of g

It is also useful to have theoretical predictions for the dimensionless conductance g to guide experiments and to develop intuition, which we describe in this section.

A. Diagrammatic method and Langevin equation

Eq. (S17) shows that one can determine g from the variance of the total transmission T_a . The transmission variance under a finite-area illumination was calculated in Refs. 11 and 20 through diagrammatic expansion methods and in Refs. 9–11 through the Langevin equation; these results can be written as

$$\frac{\text{Var}(T_a)}{\langle T_a \rangle^2} = \frac{F_2}{N_1^{(\text{geo})} \bar{T}}, \quad F_2 = \int d\mathbf{q} \frac{I(\mathbf{q})I(-\mathbf{q})}{I_2} F(q),$$

$$F(q) = \frac{\sinh(2qL) - 2qL}{2qL \sinh^2(qL)}, \quad (S18)$$

where $I(\mathbf{q}) = (2\pi)^{-(d-1)/2} \int d\rho I(\rho) e^{i\mathbf{q}\cdot\rho}$ is the Fourier transform of the illumination intensity profile $I(\rho)$ in the $d-1$ transverse dimensions, $I_2 \equiv \int d\rho I^2(\rho)$, L is the sample thickness, and $F(q)$ is the long-range correlation factor between two planewaves whose wavevectors differ by q ^{8,24}. The illumination area is $A_{\text{in}} \equiv [\int d\rho I(\rho)]^2/I_2$, and $N_1^{(\text{geo})}$ is the geometric number of modes within this area ($N_1^{(\text{geo})} = 2\pi A_{\text{in}}/\lambda^2$ in 3D, $N_1^{(\text{geo})} = 2A_{\text{in}}/\lambda$ in 2D). When the spot size is much larger than L , F_2 approaches $F(0) = 2/3$, and the resulting g approaches $N_1^{(\text{geo})} \bar{T}$. For a finite illumination area, F_2 is smaller than $2/3$, and g is larger than $N_1^{(\text{geo})} \bar{T}$.

Eq. (S18) applies to length scales larger than the transport mean free path $l \sim L\bar{T}$, so we expect it to fail when the illumination spot size D_{in} is comparable to or smaller than l . An empirical extrapolation to small spots was proposed in Ref. 23, where it was shown that replacing D_{in} with $D_{\text{in}} + D_{\text{min}}$ yields g 's that agree well with experimental data. Physically, this D_{min} models the broadening of the beam at the front surface of the sample as the incident wave converts from ballistic to diffusive; it is on the order of l , yet the quantitative value of D_{min} needs to be determined empirically²³ or through other assumptions²⁵.

B. Expanding waveguide model

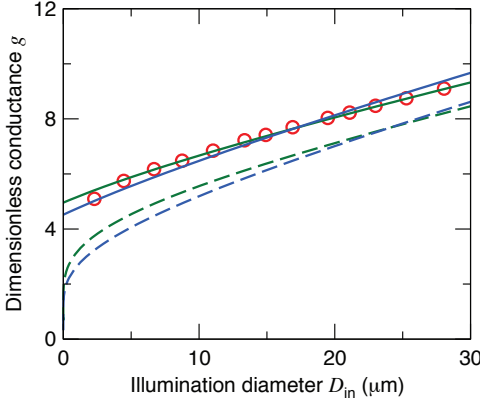
The average conductance g may also be estimated through incoherent diffusion, without accounting for interference and details of the illumination profile²³. As light penetrates into the medium, it diffuses out laterally, with a characteristic width $D(z)$ at depth z into the slab. The idea here is to model the expanding beam as an expanding waveguide with width $D(z)$. Resistance adds in series, so the conductance of such a waveguide is $g^{-1} = \sum_i g_i^{-1}$, where g_i is the conductance of a slice i of the waveguide. Each slice i has thickness $\Delta z \sim l$ and transmission $\bar{T}_i \approx (L/\Delta z)\bar{T}$, with the conductance being $g_i \approx N_i^{(\text{geo})} \bar{T}_i$; in 2D $N_i^{(\text{geo})} \approx 2D(z)/\lambda$, and in 3D $N_i^{(\text{geo})} \approx 2\pi A_i/\lambda^2$ with $A_i \approx \pi D^2(z_i)/4$. For simplicity, here we approximate the width as $D(z) \approx D_{\text{in}} + \beta z$ for some β of order unity. Then, integrating over the slices yields

$$g \approx \begin{cases} \frac{2\beta L}{\lambda \ln[1 + (\beta L/D_{\text{in}})]} \bar{T} & \text{in 2D,} \\ \frac{\pi^2}{2} \frac{D_{\text{in}}^2 + \beta D_{\text{in}} L}{\lambda^2} \bar{T} & \text{in 3D,} \end{cases} \quad (S19a)$$

with $\bar{T} \sim l/L$. This simple model illustrates how g depends on the spot size and sample thickness. As in the previous section, one needs to make the replacement $D_{\text{in}} \rightarrow D_{\text{in}} + D_{\text{min}}$ for small illumination spots.

Eq. (S19b) may be written as $g = N_1 \bar{T}$ where $N_1 = 2\pi A_{\text{eff}}/\lambda^2$ is the geometric number of modes in an effective area $A_{\text{eff}} = \pi(D_{\text{in}}^2 + \beta D_{\text{in}} L)/4$ that is larger than the illumination area $A_{\text{in}} \approx \pi D_{\text{in}}^2/4$ but smaller than the output area $A_{\text{out}} \approx \pi(D_{\text{in}} + \beta L)^2/4$. Note that when the illumination spot is small (when $D_{\text{in}} \ll L$), g becomes independent of the sample thickness L as it is dominated by the contact resistance near the input surface. The increase from A_{in} to A_{eff} (or equivalently, from $N_1^{(\text{geo})}$ to N_1) captures the loss of input control due to the lateral spreading of the beam inside the sample.

The width $D(z)$ of the spreading beam can be defined in the same way as D_{in} and obtained from the intensity profile given by the diffusion equation. This more-precise $D(z)$ does not follow the simple expression $D_{\text{in}} + \beta z$, but we find that in the range of D_{in} and L of interest here,



Supplementary Figure 4. Numerically calculated and analytically predicted g 's in 2D. Red circles are obtained from numerical simulations. Green lines are analytical predictions using diagrammatic methods, namely Eqs. (S17), (S18), (S20), with (solid) and without (dashed) the $D_{\text{in}} \rightarrow D_{\text{in}} + D_{\text{min}}$ correction. Blue lines are the expanding waveguide model, Eq. (S19a), with (solid) and without (dashed) the correction.

numerically integrating over such $D(z)$ yields results similar to that of Eq. (S19) with $\beta \approx 1.5$. Therefore, in the following we will use Eq. (S19) with $\beta = 1.5$.

C. Numerical simulations in 2D

To validate the analytic theory and to determine the value of D_{min} , we resort to numerical simulations in 2D; simulations in 3D are desirable but prohibitively time consuming for the system size of interest here.

We simulated a disordered slab of thickness $L = 60 \mu\text{m}$ on a glass substrate ($n_{\text{out}} = 1.5$), with light incident from the air ($n_{\text{in}} = 1$). The transverse size is $W = 170 \mu\text{m}$ with periodic boundary condition. We discretize the disordered slab on a 2D grid with grid size $(\lambda/2\pi)^2$, and solve the wave equation $[\nabla^2 + (\omega/c)^2 \epsilon(\mathbf{r})] \psi(\mathbf{r}) = 0$ for the full transmission matrix of the slab at $\lambda = 532 \text{ nm}$ using the recursive Green's function method²⁶; here $\epsilon(\mathbf{r}) = n_0^2 + \delta\epsilon(\mathbf{r})$, where $n_0 = 1.4$ is chosen to be the effective index of a ZnO slab²⁷, and at each grid point $\delta\epsilon(\mathbf{r})$ is drawn randomly from the uniform distribution $[-0.9, 0.9]$; this yields an average transmission of $\bar{T} \approx 3\%$.

The full transmission matrix has $N_1 \approx 2n_{\text{in}}W/\lambda$ input modes and $N_2 \approx 2n_{\text{out}}W/\lambda$ output modes that are incoming and outgoing planewaves at different angles. We group the input modes into “macropixels,” with each macropixel consisting of m neighboring incident angles and spanning size $q = m(2\pi/W)$ in the transverse wavevector space—same as the SLM macropixels in our experiment. Projecting the N_1 input modes onto the

$M_1 = N_1/m$ macropixels yields a N_2 -by- M_1 “measured” transmission matrix. Then the illumination profile is

$$I(y) \sim \frac{\sin^2(m\pi y/W)}{\sin^2(\pi y/W)} \sim \text{sinc}^2(qy/2), \quad (\text{S20})$$

with an illumination area of $D_{\text{in}} \equiv [\int dy I(y)^2 / \int dy I^2(y)] = 3\pi/q$, similar to Eq. (S1).

From the numerically calculated transmission matrices, we obtain the dimensionless conductance g for different macropixel sizes (corresponding to different illumination spots sizes); here g is calculated via Eq. (S17) using 1000 realizations of disordered slabs. The analytical predictions of g are compared to the simulation results in Supplementary Fig. 4, for the range of D_{in} comparable to our experiment. With the diagrammatic method [Eqs. (S17), (S18), (S20)], the analytical prediction agrees very well with the simulation results once the small-spot correction $D_{\text{in}} \rightarrow D_{\text{in}} + D_{\text{min}}$ is applied; here $D_{\text{min}} = 3.4L\bar{T}$ is obtained via a least-squares fitting. We also plot the expanding waveguide model [Eqs. (S19a)] with $\beta = 1.5$ and the same value of D_{min} , which yields similar results.

D. Estimations of g in the experiment

We now apply the analytic predictions for the 3D geometry in our experiment. The predicted g from diagrammatic methods [Eqs. (S17), (S18), (S1)] and from the expanding waveguide model [Eq. (S19b)] for the illumination diameters in our experiment are listed in Supplementary Table 2. Here we use the values of $D_{\text{min}} = 3.4L\bar{T}$ and β that are pre-determined from 2D simulations. These analytic predictions agree with the experimentally measured values to within $\approx 20\%$; the residual difference may arise from errors in D_{in} (e.g. if the sample surface is not exactly at the focal point), variation of the sample thickness and \bar{T} , or from the approximations used in the theory.

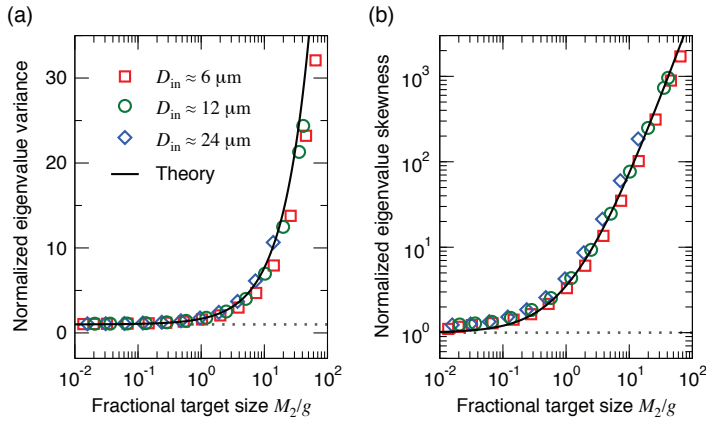
In Supplementary Fig. 5, we plot the normalized eigenvalue variance and skewness (same as Fig. 2 of the main text) as a function of M_2/g using the average g predicted by theory. The agreement between theory and experiment is still quite acceptable, showing the robustness of the scaling laws.

| | $D_{\text{in}} \approx 6 \mu\text{m}$ | $D_{\text{in}} \approx 12 \mu\text{m}$ | $D_{\text{in}} \approx 24 \mu\text{m}$ |
|---------------|---------------------------------------|--|--|
| Diag. method | 678 | 1043 | 1837 |
| Expan. waveg. | 642 | 1014 | 1866 |

Supplementary Table 2. Theoretical predictions of g using diagrammatic methods, Eqs. (S17), (S18), (S1) and the expanding waveguide model, Eq. (S19b).

¹ S. M. Popoff, G. Lerosey, R. Carminati, M. Fink, A. C. Boccara, and S. Gigan, Phys. Rev. Lett. **104**, 100601

(2010).



Supplementary Figure 5. Same plot as Fig. 2 of the main text but using the theoretically predicted g instead of the experimentally measured g .

- ² S. M. Popoff, G. Lerosey, M. Fink, A. C. Boccara, and S. Gigan, *New J. Phys.* **13** (2011).
- ³ I. M. Vellekoop and A. P. Mosk, *Opt. Commun.* **281**, 3071 (2008).
- ⁴ R. Sarma, A. G. Yamilov, S. Petrenko, Y. Bromberg, and H. Cao, *Phys. Rev. Lett.* **117**, 086803 (2016).
- ⁵ S. G. Johnson, The NLopt nonlinear-optimization package, <http://ab-initio.mit.edu/nlopt>.
- ⁶ J. Nocedal, *Math. Comput.* **35**, 773 (1980).
- ⁷ D. C. Liu and J. Nocedal, *Math. Program.* **45**, 503 (1989).
- ⁸ S. Feng, C. Kane, P. A. Lee, and A. D. Stone, *Phys. Rev. Lett.* **61**, 834 (1988).
- ⁹ R. Pnini and B. Shapiro, *Phys. Rev. B* **39**, 6986 (1989).
- ¹⁰ J. F. de Boer, M. P. van Albada, and A. Lagendijk, *Phys. Rev. B* **45**, 658 (1992).
- ¹¹ J. F. de Boer, *Optical fluctuations on the transmission and*

reflection of mesoscopic systems, Ph.D. thesis, University of Amsterdam (1995).

- ¹² P. A. Mello, E. Akkermans, and B. Shapiro, *Phys. Rev. Lett.* **61**, 459 (1988).
- ¹³ P. A. Mello and A. D. Stone, *Phys. Rev. B* **44**, 3559 (1991).
- ¹⁴ R. Berkovits and S. Feng, *Phys. Rep.* **238**, 135 (1994).
- ¹⁵ E. Akkermans and G. Montambaux, “Mesoscopic physics of electrons and photons,” (Cambridge University Press, Cambridge, UK, 2007) Chap. 12.
- ¹⁶ A. Goetschy and A. D. Stone, *Phys. Rev. Lett.* **111**, 063901 (2013).
- ¹⁷ D. V. Voiculescu, K. J. Dykema, and A. Nica, *Free random variables* (American Mathematical Society, Providence, RI, USA, 1992).
- ¹⁸ A. M. Tulino and S. Verdú, *Found. Trends Commun. Inf. Theory* **1**, 1 (2004).
- ¹⁹ V. A. Marčenko and L. A. Pastur, *Math. USSR Sbornik* **1**, 457 (1967).
- ²⁰ S. M. Popoff, A. Goetschy, S. F. Liew, A. D. Stone, and H. Cao, *Phys. Rev. Lett.* **112**, 133903 (2014).
- ²¹ D. Akbulut, *Measurements of strong correlations in the transport of light through strongly scattering materials*, Ph.D. thesis, University of Twente (2013).
- ²² J. F. de Boer, M. C. W. van Rossum, M. P. van Albada, T. M. Nieuwenhuizen, and A. Lagendijk, *Phys. Rev. Lett.* **73**, 2567 (1994).
- ²³ F. Scheffold, W. Härtl, G. Maret, and E. Matijević, *Phys. Rev. B* **56**, 10942 (1997).
- ²⁴ M. J. Stephen and G. Cwilich, *Phys. Rev. Lett.* **59**, 285 (1987).
- ²⁵ A. García-Martín, F. Scheffold, M. Nieto-Vesperinas, and J. J. Sáenz, *Phys. Rev. Lett.* **88**, 143901 (2002).
- ²⁶ H. U. Baranger, D. P. DiVincenzo, R. A. Jalabert, and A. D. Stone, *Phys. Rev. B* **44**, 10637 (1991).
- ²⁷ I. M. Vellekoop, E. G. van Putten, A. Lagendijk, and A. P. Mosk, *Opt. Express* **16**, 67 (2008).